

Article

A Room Temperature Trimethylamine Gas Sensor Based on Electrospun Molybdenum Oxide Nanofibers/ $\text{Ti}_3\text{C}_2\text{T}_x$ MXene Heterojunction

Shiteng Ma, Jingyu Guo, Hao Zhang, Xingyan Shao and Dongzhi Zhang * 

College of Control Science and Engineering, China University of Petroleum (East China), Qingdao 266580, China; mashiteng89@163.com (S.M.); guojingyu1997@126.com (J.G.); zhshy2020zh@163.com (H.Z.); shao2053850672@163.com (X.S.)

* Correspondence: dzzhang@upc.edu.cn; Tel.: +86-532-86982928; Fax: +86-532-86981335

Abstract: The combination of two-dimensional material MXene and one-dimensional metal oxide semiconductor can improve the carrier transmission rate, which can effectively improve sensing performance. We prepared a trimethylamine gas sensor based on MoO_3 nanofibers and layered $\text{Ti}_3\text{C}_2\text{T}_x$ MXene. Using electrospinning and chemical etching methods, one-dimensional MoO_3 nanofibers and two-dimensional $\text{Ti}_3\text{C}_2\text{T}_x$ MXene nanosheets were prepared, respectively, and the composites were characterized via XPS, SEM, and TEM. The $\text{Ti}_3\text{C}_2\text{T}_x$ MXene– MoO_3 composite material exhibits excellent room-temperature response characteristics to trimethylamine gas, showing high response (up to four for 2 ppm trimethylamine gas) and rapid response–recovery time (10 s/7 s). Further, we have studied the possible sensitivity mechanism of the sensor. The $\text{Ti}_3\text{C}_2\text{T}_x$ MXene– MoO_3 composite material has a larger specific surface area and more abundant active sites, combined with p–n heterojunction, which effectively improves the sensitivity of the sensor. Because of its low detection limit and high stability, it has the potential to be applied in the detection system of trimethylamine as a biomarker in exhaled air.



Citation: Ma, S.; Guo, J.; Zhang, H.; Shao, X.; Zhang, D. A Room Temperature Trimethylamine Gas Sensor Based on Electrospun Molybdenum Oxide Nanofibers/ $\text{Ti}_3\text{C}_2\text{T}_x$ MXene Heterojunction. *Nanomaterials* **2024**, *14*, 537. <https://doi.org/10.3390/nano14060537>

Academic Editor: Antonella Macagnano

Received: 6 February 2024
Revised: 9 March 2024
Accepted: 12 March 2024
Published: 18 March 2024



Copyright: © 2024 by the authors. Licensee MDPI, Basel, Switzerland. This article is an open access article distributed under the terms and conditions of the Creative Commons Attribution (CC BY) license (<https://creativecommons.org/licenses/by/4.0/>).

Keywords: electrospinning; MoO_3 nanofibers; $\text{Ti}_3\text{C}_2\text{T}_x$ MXene; trimethylamine sensor; p–n heterojunction

1. Introduction

With the rapid development of science and technology and the improvement of people's living needs, the requirement for high-performance sensors has become increasingly urgent [1]. Trimethylamine (TMA) is a common toxic gas that causes serious damage to the eyes, nose, and skin. In addition, prolonged exposure may seriously affect the nervous system [2]. Therefore, it is very important to prepare new sensitive materials and develop new preparation technology to improve the high-performance detection of TMA. In daily life, TMA can be utilized as a biomarker to evaluate the freshness of fish and other seafood. Moreover, TMA is often used to assess the degree of spoilage in seafood. This is because, after the death of the seafood, the concentration of TMA will increase correspondingly with the breakdown of trimethyl-N-oxide. When the concentration of TMA exceeds 10 ppm, it is generally regarded as being rotten [3]. In addition, some patients with certain diseases, such as trimethylaminuria, are unable to metabolize trimethylamine, leading to its elimination from the body through sweat, urine, and exhaled breath [4]. Therefore, detecting the concentration of TMA in exhaled breath can serve as a diagnostic method for diseases such as renal disorders and trimethylaminuria. Zhang et al. developed a $\text{MoO}_3/\text{V}_2\text{O}_5$ TMA gas sensor for disease detection using a hydrothermal synthesis method. This sensor has the potential for rapid detection of TMA at room temperature, showing great promise in non-invasive disease diagnosis [5]. Therefore, TMA concentration detection is an important index in seafood deterioration evaluation and human health monitoring, and it is necessary to develop a high-performance TMA sensor.

In previous studies, metal oxide semiconductor (MOS) materials have been extensively utilized in the construction of gas sensors, such as SnO_2 , In_2O_3 , Fe_2O_3 , and Co_3O_4 , owing to their advantages like low production cost, fast response, miniaturization, and good reliability [6–9]. Molybdenum trioxide (MoO_3) is a typical N-type semiconductor gas-sensitive material, and its surface contains a multitude of acidic sites that can react with basic TMA, which makes it an important material for TMA detection [10]. For example, Shen et al. synthesized MoO_3 nanosheets using the solvothermal method. The porous nanosheet TMA sensor has more oxygen vacancies, so the response value to 50 ppm TMA at a lower operating temperature (133 °C) is as high as 198 [11]. Zhou et al. synthesized $\text{MoSe}_2/\text{MoO}_3$ composite material using a two-step hydrothermal method, which exhibited excellent sensing performance towards TMA gas. The response/recovery time reached the sub-second level, with a low detection limit down to the ppb range [12]. Yan et al. designed a porous, hollow $\text{Co}_3\text{O}_4@\text{ZnO}$ structure for the TMA sensor using a simple ZIF-67/ZIF8-derived method. The sensor shows good TMA resistance sensing performance with high sensitivity and fast response/recovery time. The sensor also has better baseline stability [13].

In recent years, numerous scholars have conducted in-depth research on the applications of two-dimensional nanomaterials such as graphene [14], molybdenum disulfide (MoS_2) [15], and tin selenide (SnSe_2) [16] in the field of sensors. Their characteristics of high specific surface area and high surface activity make them extremely important functional materials in the field of sensor-sensitive materials [17,18]. MXene is an emerging two-dimensional transition metal carbide or nitride composed of transition metal nitride, carbide, and carbonitride. Its unique properties have attracted much attention in the field of nanotechnology, and it has been used to distinguish various inorganic gases and volatile organic compounds through chemical etching Ti_3AlC_2 [19–21]. $\text{Ti}_3\text{C}_2\text{T}_x$ is one of the most extensively studied MXenes, which possesses a high specific surface area and conductivity and is capable of adsorbing numerous functional groups on its surface [22,23]. $\text{Ti}_3\text{C}_2\text{T}_x$ MXene provides a matrix with unique gas adsorption capacity and good electrical conductivity, enabling heterojunction-based room-temperature sensing [24]. With these unique advantages, $\text{Ti}_3\text{C}_2\text{T}_x$ MXene is widely used for gas detection at room temperature. He et al. successfully synthesized MXene modified using SnO_2 nanoparticles via a hydrothermal method. The formed MXene/ SnO_2 -based heterojunction sensor has excellent sensitivity to different NH_3 concentrations from 0.5 to 100 ppm at room temperature [24]. Zhang et al. prepared a high-performance trace ammonia sensor based on (001) $\text{TiO}_2/\text{MXene}$. Using the synergistic effect of TiO_2 and MXene (001) crystal surface, the sensing performance of the sensor is effectively enhanced, and the ultralow detection limit of 156 ppt is achieved, which can conveniently and economically detect food deterioration [25]. The MXene and SnO_2 have different Fermi levels that can drive the charge transfer at the heterojunction interface, enrich the electrons on the surface area of SnO_2 , and improve the sensitivity of the $\text{Ti}_3\text{C}_2\text{T}_x$ MXene– SnO_2 -based gas sensor.

In this study, $\text{Ti}_3\text{C}_2\text{T}_x$ MXene– MoO_3 composite material was prepared using electrospinning and chemical etching methods, forming a p–n heterojunction. The $\text{Ti}_3\text{C}_2\text{T}_x$ MXene– MoO_3 composite material was characterized using SEM, XPS, XRD, and other methods. The sensing performance of the sensor was thoroughly investigated, and the sensor exhibited excellent sensitivity, rapid response, outstanding selectivity, and good long-term stability to TMA. Through the analysis of the sensing mechanism of the sensor, it was further demonstrated that heterojunction could effectively enhance gas sensing performance. In addition, a TMA alarm detection system was constructed based on the $\text{Ti}_3\text{C}_2\text{T}_x$ MXene– MoO_3 sensor, achieving rapid alarm for TMA exceeding the limit. This study provides a theoretical basis and solutions for the development of non-invasive disease detection and food spoilage detection.

2. Experimental

2.1. Materials

The ammonium heptamolybdate $[(\text{NH}_4)_6\text{Mo}_7\text{O}_{24}\cdot 4\text{H}_2\text{O}]$ (99%, CAS: 12054-85-2), polyvinylpyrrolidone (PVP, $M_w = 1,300,000$, CAS: 9003-39-8), hydrochloric acid (HCl, analytical grade, CAS: 7647-01-0), titanium aluminum carbide powder (Ti_3AlC_2 , CAS: 196506-01-1), anhydrous ethanol ($\text{CH}_3\text{CH}_2\text{OH}$, 99.7%, CAS: 64-17-5), N,N-dimethylformamide (DMF, 99.5%, CAS: 68-12-2), and lithium fluoride (LiF, 99%, CAS: 7789-24-4) used in this study were all purchased from National Pharmaceutical Chemistry Reagents.

2.2. Material Synthesis

The MoO_3 nanofibers were prepared using a combination of electrospinning and calcination. Firstly, DMF and anhydrous ethanol were mixed in a ratio of 1:1. Then, 0.8 g of PVP and 0.3 g of ammonium heptamolybdate were dissolved in 20 mL of the mixed solvent, and the solution was stirred magnetically at $60\text{ }^\circ\text{C}$ for 12 h. When the solution became transparent, the electrospinning precursor was obtained. Subsequently, the prepared precursor was moved to a syringe (No. 21) and subjected to a voltage of 16 kV (feeding rate of 0.707 mL/h and distance of 15 cm) to obtain ammonium heptamolybdate/PVP nanofibers. Finally, the composite nanofibers were calcined at $500\text{ }^\circ\text{C}$ for 2 h to completely remove the organic polymer components.

Delaminated $\text{Ti}_3\text{C}_2\text{T}_x$ MXene with great dispersion in water was synthesized through etching Ti_3AlC_2 [19], as shown in Figure 1. The MoO_3 nanofibers and $\text{Ti}_3\text{C}_2\text{T}_x$ MXene solution were dissolved in ethanol with magnetic stirring, and the $\text{Ti}_3\text{C}_2\text{T}_x$ MXene– MoO_3 mixture suspension was obtained for subsequent use.

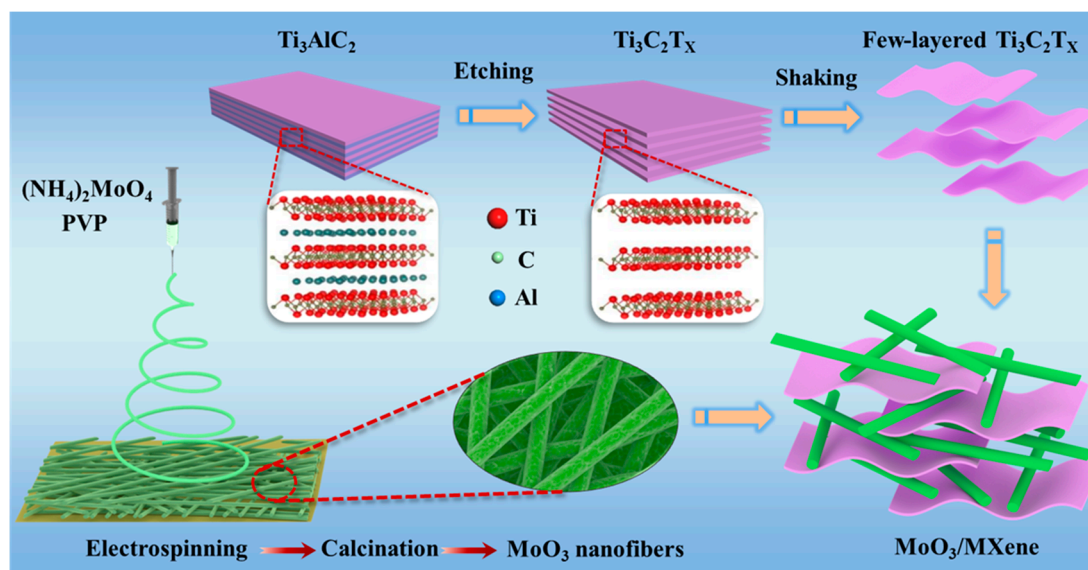


Figure 1. The preparation process of the $\text{Ti}_3\text{C}_2\text{T}_x$ MXene– MoO_3 nanocomposite.

2.3. Test Device

The $\text{Ti}_3\text{C}_2\text{T}_x$ MXene– MoO_3 hybrid suspension was assembled on the electrode surface using a layer-by-layer coating technique [26–28]. The material was fully and evenly dissolved in volatile ethanol, ground with a mortar for 20 min, and then subjected to ultrasonicated to disperse the sample more evenly in ethanol. Finally, the surface of the sensor is coated with composite sensing materials layer by layer using a brush and dried for aging so that the $\text{Ti}_3\text{C}_2\text{T}_x$ MXene– MoO_3 sensor is prepared.

The TMA test system is shown in Figure 2, which mainly includes TMA, N_2 , gas flow controller, test chamber, $\text{Ti}_3\text{C}_2\text{T}_x$ MXene– MoO_3 sensor, data logger, and host computer. A data logger (Agilent 34970A) is used to acquire the $\text{Ti}_3\text{C}_2\text{T}_x$ MXene– MoO_3 sensor response.

The sensor was tested in a 750 mL closed gas chamber. A certain volume of standard TMA gas is extracted with a syringe and mixed with pure air to obtain different concentrations (0.2–10 ppm) of TMA gas. Based on the real-time monitoring of the Agilent 34970a, the change in the resistance of the sensor under TMA gas is recorded, and the test results are displayed on the computer. During the test, the sensor is first placed in an N₂ environment to obtain a stable fundamental resistance.

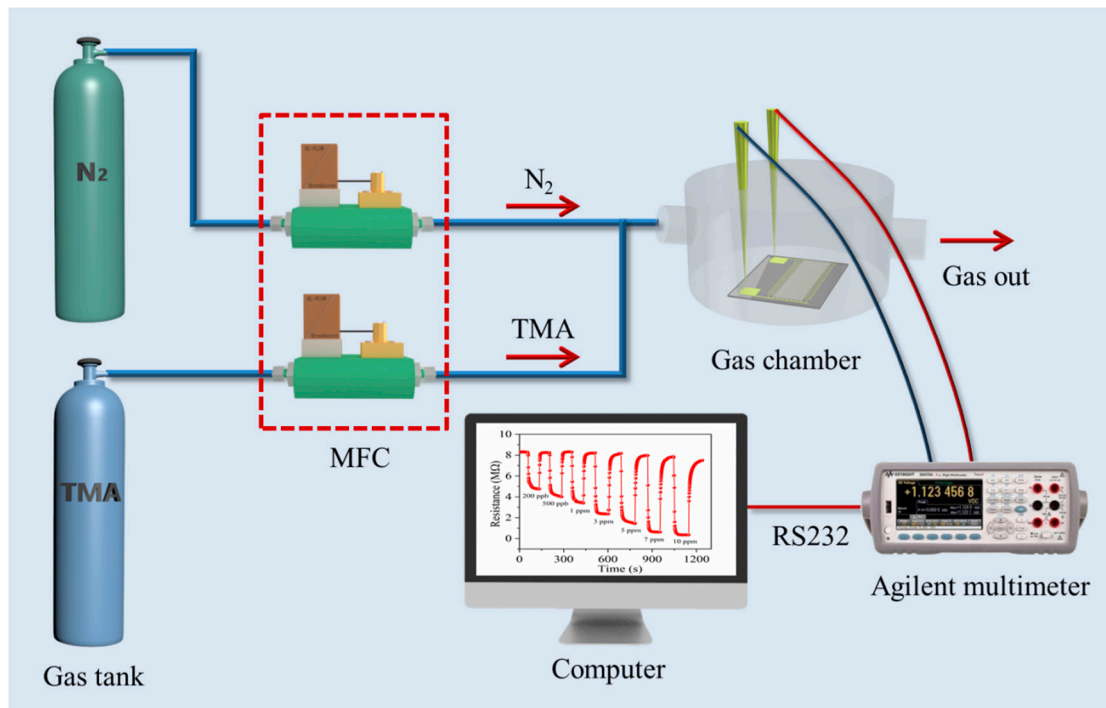


Figure 2. Schematic illustration of the TMA-sensing measurement system.

During the testing phase of the sensor, its response (S) is defined as $|R_a - R_g| / R_a \times 100\%$, where R_g and R_a are the resistance values of the sensor before and after the introduction of the target gas molecule, respectively. The sensor response and recovery time are the time it takes for its resistance value to reach 90% of the total resistance variation range.

2.4. Characterization

The samples were imaged using a field emission scanning electron microscope (Hitachi SU8020, the equipment is manufactured by Hitachi High-Tech Co., Ltd. in Tokyo, Japan) and a transmission electron microscope (TEM, JEM-2100, the equipment is manufactured by Hitachi High-Tech Co., Ltd., Tokyo, Japan). MXene, MoO₃, and Ti₃C₂T_x MXene–MoO₃ composites were characterized using a Bruker D8 ADVANCE (The device is manufactured by Bruker Corporation, Billerica, MA, USA) phase X-ray diffractometer (XRD). X-ray photoelectron spectroscopy (XPS) was conducted using a Thermo escalab 250Xi scanning (TEC, USA, the equipment is manufactured by Thermo Fisher Scientific, Waltham, MA, USA).

3. Results and Discussion

3.1. Sample Characterization

The XRD analysis of Ti₃C₂T_x MXene, MoO₃, and Ti₃C₂T_x MXene–MoO₃ nanocomposites was performed using an X-ray diffractometer (Rigaku D/Max 2500PC). As illustrated in Figure 3, the diffraction peaks observed in the acquired samples are effectively matched with the orthorhombic phase of MoO₃ (JCPDS No.89-5108) and Ti₃C₂T_x MXene (JCPDS No.29-0095). The diffraction peaks of MoO₃ are centered at $2\theta = 13.2^\circ, 23.8^\circ, 26.1^\circ, 27.4^\circ, 38.6^\circ, 42.3^\circ, 46.6^\circ, \text{ and } 53.3^\circ$, corresponding to the (020), (110), (040), (021), (060), (141), (200), and (211) crystal planes, respectively [29]. During the calcination process, the complete

elimination of PVP ensured the absence of any additional impurity peaks in the observed spectrum. Three high-intensity diffraction peaks can be observed, which indicates that MoO_3 is a highly ordered orthorhombic crystal. The blue curve represents the widened peak observed at 7.7° , indicative of the (002) plane of $\text{Ti}_3\text{C}_2\text{T}_x$ MXene, characterized by a lattice constant of 14.3 \AA [30]. The X-ray diffraction (XRD) examination of the $\text{Ti}_3\text{C}_2\text{T}_x$ MXene– MoO_3 manifests congruent characteristic peaks corresponding to both MoO_3 and $\text{Ti}_3\text{C}_2\text{T}_x$ MXene, providing robust confirmation regarding the successful synthesis of the $\text{Ti}_3\text{C}_2\text{T}_x$ MXene– MoO_3 nanocomposite. The observed identical peaks in the XRD spectrum affirm the efficacious formation of the composite material, underscoring the precision and effectiveness of the synthesis process employed.

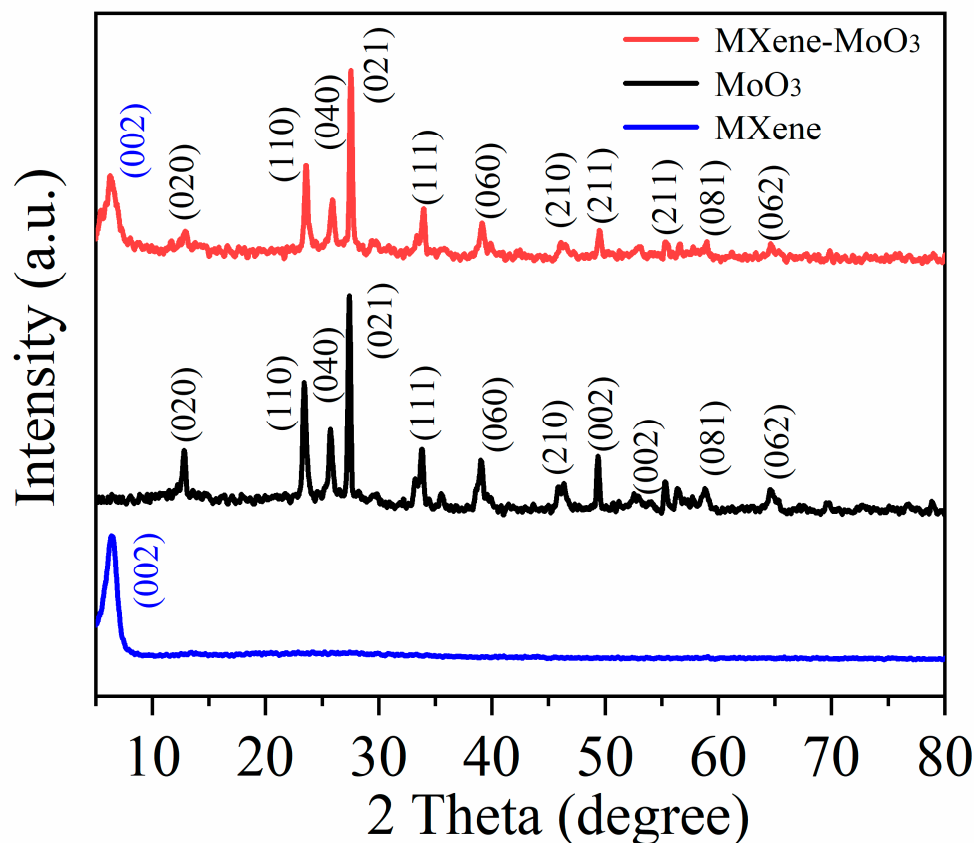


Figure 3. XRD pattern of the $\text{Ti}_3\text{C}_2\text{T}_x$ MXene– MoO_3 nanocomposite.

XPS characterization is used to determine the surface chemical composition and element valence of $\text{Ti}_3\text{C}_2\text{T}_x$ MXene– MoO_3 . In the C 1s spectrum (Figure 4a), four distinctive fitting peaks are discernible at 282.6, 284.7, 286.6, and 288.9 eV, respectively, representing the C–Ti, C–C, C–O, and C–F bonds, thereby confirming the characteristic carbon bonding in $\text{Ti}_3\text{C}_2\text{T}_x$ [31]. The Ti 2p spectrum exhibits four identifiable peaks, as anticipated in Figure 4b. The binding energies at 454.1, 457.7, 459.3, and 463.5 eV are attributed to Ti–C ($2p_{3/2}$), Ti (II) ($2p_{3/2}$), Ti–C ($2p_{1/2}$), and Ti–O ($2p_{1/2}$) bonds, respectively [32]. Figure 4c shows the Mo 3d energy level spectrum. The prominent symmetrical peaks, with a center at 235.6 eV and 232.5 eV, are indicative of Mo $3d_{5/2}$ and Mo $3d_{3/2}$ states within MoO_3 , respectively. The XPS spectrum of the O element, depicted in Figure 4d, illustrates a low binding energy peak at 529.2 eV, attributed to the Mo–O bond within MoO_3 , while a high binding energy peak at 530.7 eV signifies the presence of oxygen adsorbed on the sample’s surface [29].

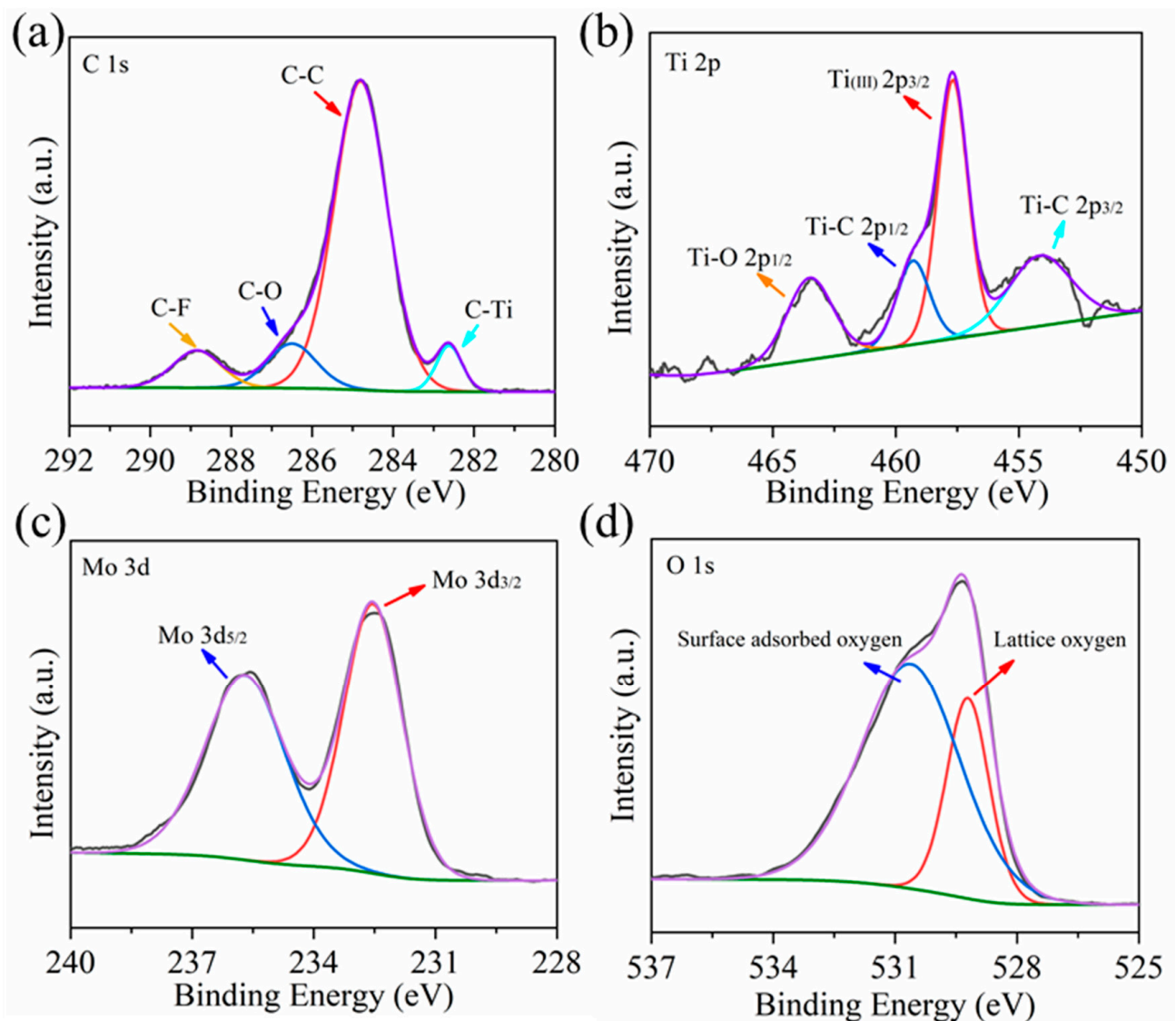


Figure 4. XPS spectra of $\text{Ti}_3\text{C}_2\text{T}_x$ MXene– MoO_3 sample: (a) C 1s core level spectrum, (b) Ti 2p core level spectrum, (c) Mo 3d core level spectrum, and (d) O 1s core level spectrum.

Figure 5 shows the scanning electron microscope and transmission electron microscope images of MoO_3 , $\text{Ti}_3\text{C}_2\text{T}_x$ MXene, and $\text{Ti}_3\text{C}_2\text{T}_x$ MXene– MoO_3 heterostructure. Figure 5a is an image of MoO_3 nanofibers. The diameter of the fibers is about 500 nm, and they are composed of closely arranged tiny particles. Figure 5b shows the typical accordion-like structure of $\text{Ti}_3\text{C}_2\text{T}_x$ MXene. Figure 5c,d are the SEM images of the $\text{Ti}_3\text{C}_2\text{T}_x$ MXene– MoO_3 composite after ultrasonic treatment. It can be seen that the MoO_3 nanofibers and the flake-like $\text{Ti}_3\text{C}_2\text{T}_x$ MXene are tightly combined after the composite material is ultrasonically processed. Figure 5e,f show TEM images of $\text{Ti}_3\text{C}_2\text{T}_x$ MXene– MoO_3 . From Figure 5e, we can observe the composite morphology of nanofibers with a diameter of 500 nm and $\text{Ti}_3\text{C}_2\text{T}_x$ MXene. After magnifying the TEM image of $\text{Ti}_3\text{C}_2\text{T}_x$ MXene, the existence of lattice fringes can be clearly observed. For example, the crystal spacing of 0.26 nm corresponds to the 101 crystal plane of $\text{Ti}_3\text{C}_2\text{T}_x$ MXene. In conclusion, the SEM and TEM characterization images clearly demonstrate the effective synthesis of the $\text{Ti}_3\text{C}_2\text{T}_x$ MXene– MoO_3 heterostructure. The SEM and TEM analyses provide compelling visual evidence, showcasing the successful fabrication of the heterostructure.

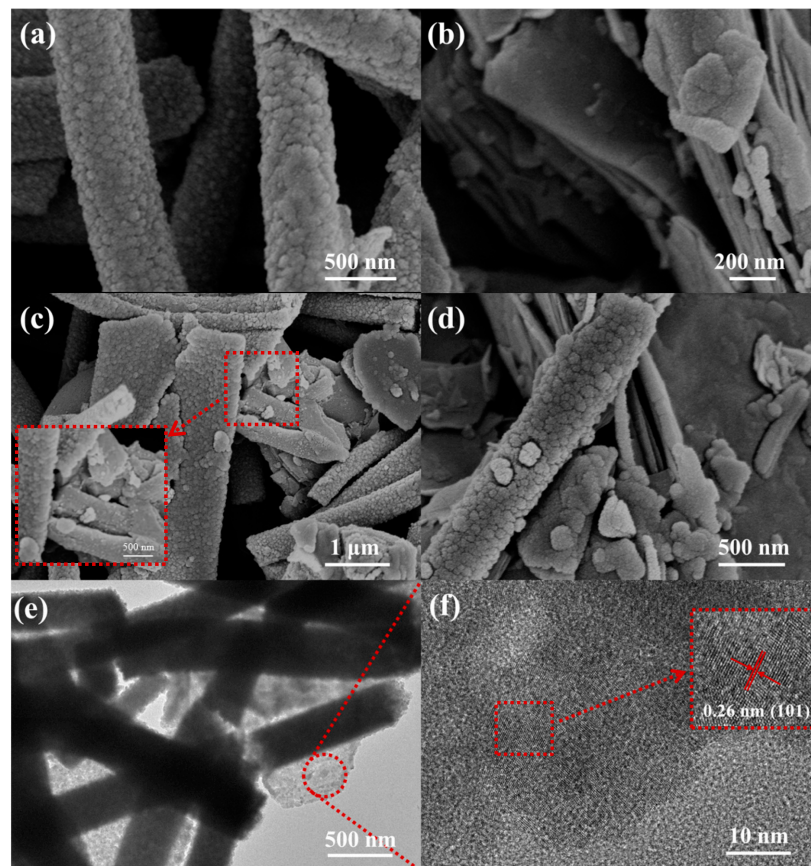


Figure 5. SEM images of (a) MoO₃ nanofibers, (b) accordion-like MXene, and (c,d) Ti₃C₂T_x MXene–MoO₃ nanocomposite. (e,f) TEM images of Ti₃C₂T_x MXene–MoO₃ nanocomposite.

3.2. TMA Sensing Properties

To comprehensively assess the gas sensing capabilities of the Ti₃C₂T_x MXene–MoO₃ composite materials, a comprehensive array of measurements was undertaken to evaluate various parameters, including sensor sensitivity, stability, response time, and additional performance indicators. This thorough investigation involved detailed analyses aimed at elucidating the sensor's effectiveness in detecting target gases, ensuring a comprehensive understanding of its operational characteristics. The entire testing process was conducted at room temperature (25 °C), with a relative humidity (RH) of 67% in the testing environment. First, we explored the effect of different masses of Ti₃C₂T_x MXene doping on sensor performance. As shown in Figure 6a, we measured the response of 0%, 5%, 10%, 15%, and 20% mass. When the sensor is exposed to TMA gas, the resistance will be significantly reduced. This phenomenon indicates that the Ti₃C₂T_x MXene–MoO₃ composite exhibits typical n-type behavior. The data reveal that among the tested compositions, the 10% Ti₃C₂T_x MXene–MoO₃ exhibits the most elevated response magnitude and demonstrates the swiftest response and recovery times. However, Ti₃C₂T_x MXene exhibits p-type behavior for TMA, and the response value is not high. This is because MXene acts as an electron donor rather than the main sensing material, so the appropriate MXene doping amount determines the final performance of the sensor. Then, we tested the performance of the 10% Ti₃C₂T_x MXene–MoO₃ under different TMA gas concentrations. The response of the Ti₃C₂T_x MXene–MoO₃ sensor was obtained by adjusting the concentration of TMA gas in the test chamber through the gas flow controller. The findings are depicted in the graphical representation presented in Figure 6b. The sensor demonstrates good response and recovery characteristics for different concentrations of TMA gas, with the detection limit as low as 0.2 ppm. In this work, the detection limit of the sensor is 0.2 ppm. Tests have been performed at concentrations below 0.2 ppm, and the results show that the sensor can detect

lower concentrations but inconsistently. In keeping with scientific rigor, the detection of this sensor is limited to 0.2 ppm in this article. As the concentration of TMA gas increased from 0.2 ppm to 10 ppm, the response value of the 10% $\text{Ti}_3\text{C}_2\text{T}_x$ MXene– MoO_3 sensor increased from 1.74 to 21.2. In contrast, the response value of the pure MoO_3 nanofiber gas sensor increased only from 1.33 to 10.7. It is worth noting that both the $\text{Ti}_3\text{C}_2\text{T}_x$ MXene– MoO_3 and MoO_3 sensors exhibit excellent linear relationships between their response and gas concentration, as shown in Figure 6c. The linear fitting equations are $Y = 1.9536X + 0.6267$ ($R^2 = 0.9896$) and $Y = 0.9036X + 1.0632$ ($R^2 = 0.9840$). Furthermore, the incorporation of $\text{Ti}_3\text{C}_2\text{T}_x$ MXene significantly enhances the response speed of the sensor, possibly due to its high specific surface area and surface activity. The response/recovery time of the 10% $\text{Ti}_3\text{C}_2\text{T}_x$ MXene– MoO_3 sensor to 2 ppm TMA was reduced to 10 s/7 s. Compared to the response/recovery time (32 s/23 s) of the MoO_3 gas sensor, the MXene– MoO_3 gas sensor exhibits a faster response/recovery speed in TMA gas sensing, as shown in Figure 6d. This may be attributed to the higher electron transfer efficiency and excellent conductivity of $\text{Ti}_3\text{C}_2\text{T}_x$ MXene in gas-sensitive sensing nano-composite materials.

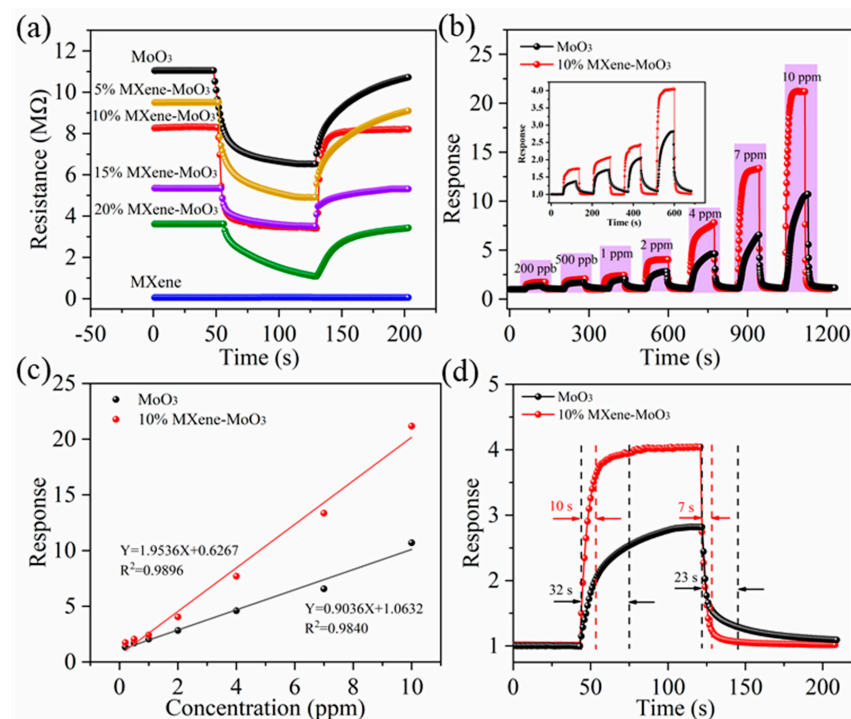


Figure 6. (a) The effect of different doping amounts of MXene on sensor performance under 1 ppm TMA gas. (b) Response curves of MoO_3 sensor and 10% $\text{Ti}_3\text{C}_2\text{T}_x$ MXene– MoO_3 sensor at 200 ppb–10 ppm TMA gas concentration. (c) Fitting relationship between gas concentrations and sensor response. (d) Response and recovery characteristics of the sensor to 2 ppm TMA gas at 25 °C.

To assess the gas selectivity of the MXene– MoO_3 sensor comprehensively, a diverse array of gases, such as hydrogen sulfide (H_2S), ethanol, nitrogen dioxide (NO_2), sulfur dioxide (SO_2), and carbon monoxide (CO), were specifically chosen for testing purposes. This meticulous selection of gases aims to provide a thorough examination of the sensor's ability to discern and respond to different gas types, thereby enhancing the depth of our understanding regarding its selective detection capabilities. When the gas concentration is uniformly 2 ppm, the 10% $\text{Ti}_3\text{C}_2\text{T}_x$ MXene– MoO_3 sensor exhibits a higher response to TMA compared to other gases, as shown in Figure 7a. This indicates that the MXene– MoO_3 sensor possesses excellent selectivity. The sensor was placed at 0.2 ppm, 2 ppm, and 10 ppm TMA gas concentrations, and the resistance curve of the sensor was recorded during the three cycles (Figure 7b). It was observed that the sensor has excellent repeatability at low concentrations of TMA gas, but the initial resistance of the sensor showed a slight shift

at the concentration of 10 ppm gas. Additionally, the long-term stability of the sensor was tested over one month. As shown in Figure 7c, during this period, the sensor's response to 2 ppm TMA gas did not exhibit significant changes, indicating excellent stability. However, the recovery of the sensor cannot be 100% after analyte removal. Subsequently, we explored the impact of ambient humidity on the sensing capabilities of the sensor. As shown in Figure 7d, the baseline resistance of the sensor (black line) decreases as humidity increases, and so does the response of the sensor (blue line), but the declining trend shows a linear relationship. In contrast to previously documented TMA sensors, the $\text{Ti}_3\text{C}_2\text{T}_x$ MXene– MoO_3 sensor presents notable advantages, including the ability to operate at low testing temperatures, specifically at room temperature. Moreover, it showcases heightened sensitivity and remarkably low detection limits, thus positioning it as a promising advancement in the field of gas sensing technology. This sensor surpasses its predecessors by offering superior performance metrics, paving the way for enhanced detection capabilities in various applications (Table 1).

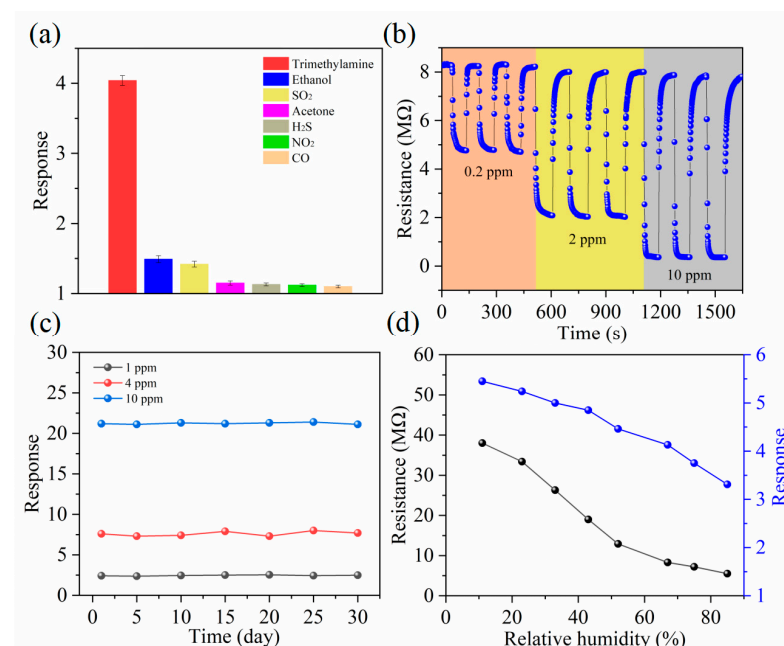


Figure 7. (a) Selectivity of the $\text{Ti}_3\text{C}_2\text{T}_x$ MXene– MoO_3 sensor toward 2 ppm of various gas species at 25 °C in 5 repeat experiments. (b) Repeatability of the $\text{Ti}_3\text{C}_2\text{T}_x$ MXene– MoO_3 sensor. (c) Long-term stability of the $\text{Ti}_3\text{C}_2\text{T}_x$ MXene– MoO_3 sensor toward 1, 4, and 10 ppm TMA gas at 25 °C. (d) Effect of relative humidity on the initial resistance and TMA-sensing properties of the $\text{Ti}_3\text{C}_2\text{T}_x$ MXene– MoO_3 sensor at 25 °C.

Table 1. Comparison of TMA sensing performances of the sensor in this work with previously reported sensors.

Materials	Fabrication Method	Conc. (ppm)	Tem. (°C)	Response	LOD (ppm)	Ref.
Pd–ZnO	Solvothermal	1	300	2.9	1	[33]
V_2O_5	Hydrothermal	100	240	2.8	10	[34]
V_2O_3 – Cu_2O	Electron beam evaporation	3	RT	1.08	3	[35]
Co_3O_4 /SnO ₂	Hydrothermal	5	175	9.3	5	[36]
MoO_3 /Bi ₂ Mo ₃ O ₁₂	Sol-gel	10	170	7.2	0.1	[37]
Rh/ZnO	Thermal evaporation	10	180	11.3	0.055	[38]
MoS_2 /SnO ₂	Hydrothermal	5	230	6	~	[39]
$\text{Ti}_3\text{C}_2\text{T}_x$ MXene– MoO_3	Electrospinning-hydrothermal	10	RT	21.2	0.5	This work

3.3. Design of TMA Concentration Alarm Circuit

Additionally, we developed an alarm circuit for the sensor that operates beyond the predefined concentration limits of TMA, serving as a safeguard mechanism. This innovative feature facilitates the generation of an alarm signal, effectively notifying users when the concentration of TMA surpasses a specified threshold. The incorporation of this over-limit alarm circuit enhances the practical utility of the sensor by ensuring timely alerts in situations where TMA concentrations exceed desired or safe levels, thereby contributing to an augmented level of safety and control in various applications. The circuit consists of a $\text{Ti}_3\text{C}_2\text{T}_x$ MXene– MoO_3 sensor, voltage comparator, alarm LED light, buzzer, switch, adjustable potentiometer, triode, resistors, capacitors, etc. Different alarm limits can be set by adjusting the resistance of the potentiometer. Figure 8a illustrates the circuit schematic of the TMA concentration detection and over-limit alarm device. Figure 8b is the physical picture of the alarm circuit. The size of the circuit is $6\text{ cm} \times 6\text{ cm}$, and it is powered using an external 5 V battery. As shown in Figure 8c, after the alarm device switch is turned on, the green LED lights up, indicating that it is working. As the concentration of TMA gas in the tested environment increases, the resistance value of the sensor also changes accordingly. When the concentration reaches 2 ppm, the TMA gas triggers the activation of the red warning indicator; the green light does not go out, indicating that the ambient TMA concentration exceeds the specified limit. This illumination serves as a visual alert, indicating the need for immediate attention or remedial action due to the elevated presence of TMA in the surroundings. This mechanism guarantees swift detection of potentially perilous TMA concentrations, fostering a proactive approach and upholding safety standards in pertinent settings. Facilitating timely recognition of elevated TMA levels empowers preemptive actions to mitigate risks and uphold regulatory safety protocols within the designated environments (Figure 8d).

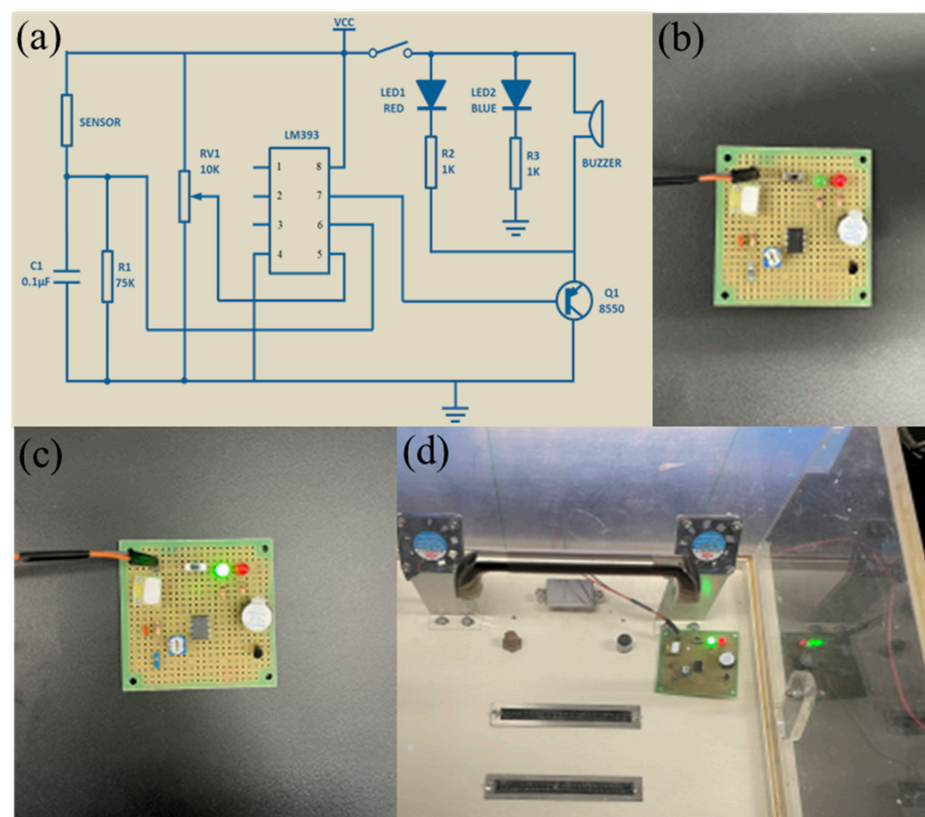
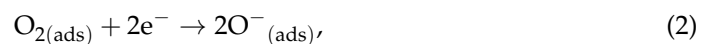


Figure 8. (a) TMA concentration over-limit alarm circuit diagram and (b) physical object. (c) Turn on the alarm circuit switch in the air environment (green light is on). (d) Alarm in a 2 ppm trimethylamine environment (red light on).

3.4. Mechanism of TMA Gas-Sensing Properties

Figure 9 shows the possible sensing mechanism of the $\text{Ti}_3\text{C}_2\text{T}_x$ MXene– MoO_3 nanocomposite sensor for TMA gas sensing. Its efficacy hinges on the efficient absorption and desorption characteristics of the sensing substance onto the surface of the MXene– MoO_3 sensing material, followed by subsequent redox reactions. This effectiveness is contingent upon the ability of the sensing substance to be readily absorbed and released from the surface of the sensing material, thereby facilitating the desired chemical reactions. The dynamic interplay between absorption, desorption, and redox processes dictates the overall performance of the sensor, underscoring the importance of these intricate surface interactions in achieving optimal sensing outcomes. This intricate balance of absorption and desorption dynamics, coupled with redox reactions, governs the sensor's ability to detect and respond to target stimuli, highlighting the significance of understanding and optimizing these surface phenomena for enhanced sensor performance. Upon exposure to air, the $\text{Ti}_3\text{C}_2\text{T}_x$ MXene– MoO_3 nanocomposite-based sensor experiences the adsorption of O_2 molecules onto the MoO_3 nanofiber surface. This process results in the entrapment of free electrons within the conduction band of MoO_3 , leading to the formation of $\text{O}^-_{(\text{ads})}$ (Equations (1) and (2)). Consequently, an electron depletion layer manifests on the nanofiber surface. Simultaneously, the transfer of holes occurs from O_2 gas molecules to the valence band of $\text{Ti}_3\text{C}_2\text{T}_x$ MXene, resulting in the formation of an augmented layer of hole accumulation on the surface of the p-type $\text{Ti}_3\text{C}_2\text{T}_x$ MXene.



and



When TMA gas molecules are adsorbed, they will consume the pre-adsorbed oxygen according to Equation (3) and release the trapped electrons back to the $\text{Ti}_3\text{C}_2\text{T}_x$ MXene– MoO_3 nanocomposite, thereby reducing the resistance value of the sensor.

Additionally, upon the convergence of p-type and n-type semiconductors, the intermingling of holes and electrons at the interface instigates the emergence of heterojunctions, representing a pivotal catalyst in amplifying the sensing proficiency of composite materials. As shown in Figure 9b, the work function of the p-type semiconductor material MXene is 4.7 eV, and the band gap is 1.14 eV, while the work function of the n-type semiconductor MoO_3 is 6.9 eV, and the band gap is 3.2 eV. It can be seen that the Fermi level of MXene is higher than that of MoO_3 . Therefore, when the two are in contact with each other in the air, electrons will transfer from MXene with a high Fermi level to MoO_3 , and the holes will move in opposite directions until the Fermi level of the two reaches equilibrium. At this time, an electron depletion layer is formed on the MXene side, an electron stacking layer is formed on the MoO_3 side, and the p–n heterojunction is also formed. When the composite material is placed in a TMA gas environment, the adsorbed oxygen reaction of the trimethylamine and the surface of the material releases electrons to the conduction band of the material, thereby enhancing the conductivity of the sensing material and decreasing the sensor resistance. As a consequence of TMA adsorption and desorption, a potential blockade arises at the interface of $\text{Ti}_3\text{C}_2\text{T}_x$ MXene and MoO_3 , consequently augmenting the quantity of adsorbed oxygen species. In a TMA environment, the $\text{Ti}_3\text{C}_2\text{T}_x$ MXene– MoO_3 hybrid composite sensor undergoes a reaction with the TMA gas and the surface-bound oxygen, liberating electrons and consequently causing a reduction in the thickness of the depletion layer, thereby amplifying the sensor's responsiveness. Additionally, the unique structures of one-dimensional nanofibers and two-dimensional layered composite materials endow them with higher electron transfer efficiency and larger specific surface areas. By capitalizing on these benefits, the sensor gains access to an increased number of reaction sites, consequently augmenting its sensing capabilities. This strategic utilization

of its advantageous features serves to amplify the sensor's performance in detecting and responding to target stimuli. By leveraging these inherent strengths, the sensor effectively maximizes its potential for accurate and reliable sensing across various applications. This optimized utilization of resources and functionalities underscores the sensor's capacity to deliver enhanced performance and efficacy in sensing.

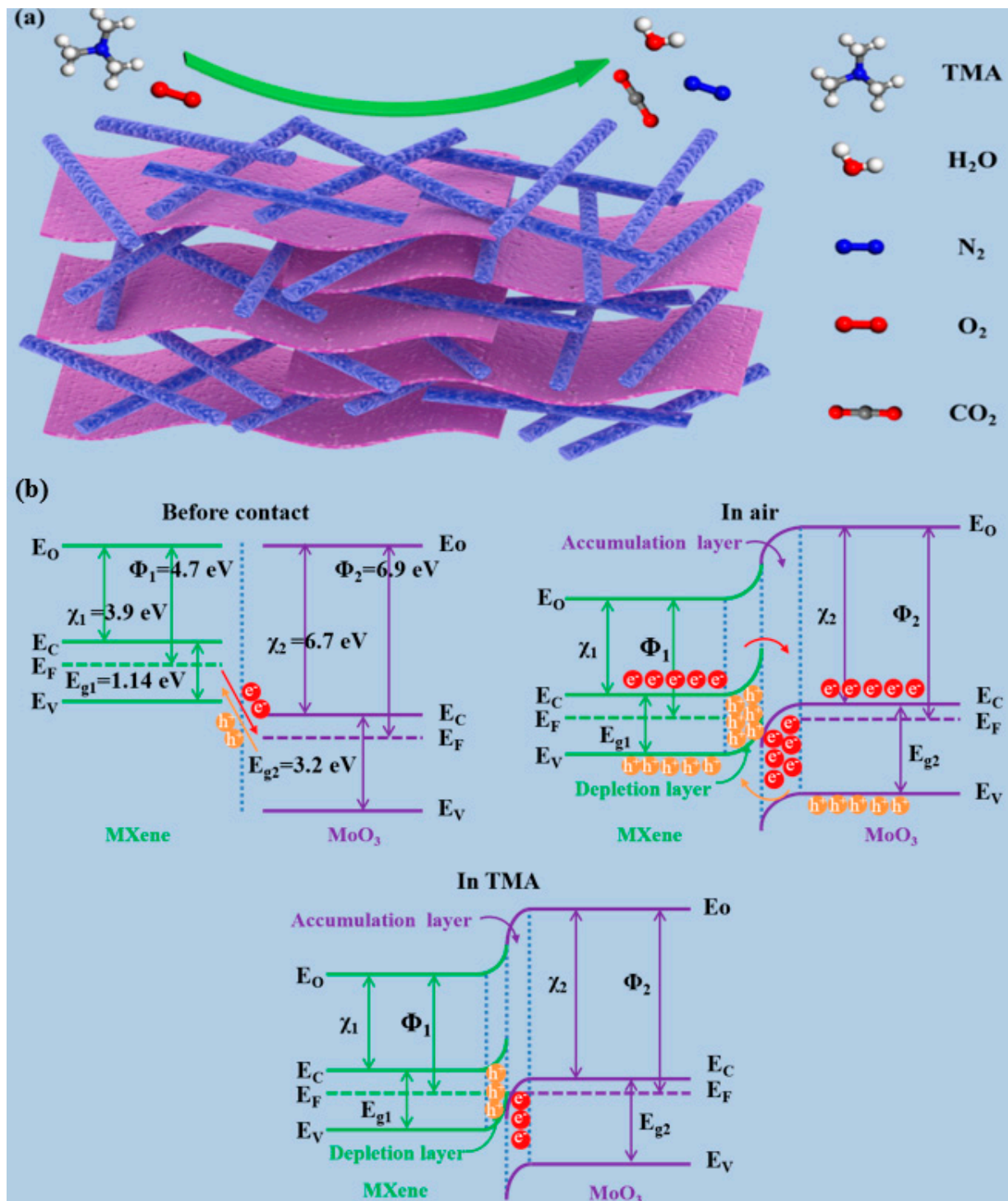


Figure 9. (a) Schematic of $\text{Ti}_3\text{C}_2\text{T}_x$ MXene– MoO_3 heterostructure in TMA gas. (b) Energy band structure diagram of $\text{Ti}_3\text{C}_2\text{T}_x$ MXene– MoO_3 heterojunction.

4. Conclusions

In summary, we have proposed a $\text{Ti}_3\text{C}_2\text{T}_x$ MXene– MoO_3 gas sensor and demonstrated its excellent sensing performance toward TMA gas at room temperature. Furthermore, a possible sensing mechanism for this sensor has been proposed. MoO_3 nanofibers were prepared through electrospinning, with a diameter of about 500 nm, and layered $\text{Ti}_3\text{C}_2\text{T}_x$ MXene nanosheets were prepared using a classic etching method. $\text{Ti}_3\text{C}_2\text{T}_x$ MXene– MoO_3 nanocomposites have extremely low detection limits for trimethylamine gas, excellent selectivity, and extremely fast response/recovery characteristics (10 s/7 s). The remarkable sensing prowess of the $\text{Ti}_3\text{C}_2\text{T}_x$ MXene– MoO_3 sensor in detecting trimethylamine gas is predominantly due to the distinctive morphological characteristics characterized using one-dimensional and two-dimensional structures coupled with the establishment of a p–n heterojunction. In addition, we designed a trimethylamine gas concentration alarm system based on $\text{Ti}_3\text{C}_2\text{T}_x$ MXene– MoO_3 sensor and achieved good application effects. Moreover, a potential sensing mechanism has been suggested for this sensor. This proposed mechanism offers insight into the underlying processes through which the sensor detects and responds to the target gases. By delineating the possible pathways and interactions involved in gas sensing, this theoretical framework aids in elucidating the sensor's operational principles and enhancing our understanding of its functionality. TMA sensors can detect TMA gas in spoiled seafood and exhaled breath with ultrahigh sensitivity and selectivity. It has potential applications in human health monitoring, food safety, and environmental assessment.

Author Contributions: Conceptualization, S.M. and J.G.; methodology, S.M.; validation, J.G., H.Z. and X.S.; investigation, S.M.; resources, J.G., H.Z. and X.S.; data curation, S.M.; writing—original draft preparation, S.M.; writing—review and editing, D.Z.; visualization, S.M.; supervision, D.Z. All authors have read and agreed to the published version of the manuscript.

Funding: This work was supported by the Special Foundation of the Taishan Scholar Project (tsqn202211077), the Shandong Provincial Natural Science Foundation (ZR2023ME118), and the Natural Science Foundation of Qingdao City (23-2-1-219-zyyd-jch).

Data Availability Statement: The data that has been used is confidential.

Conflicts of Interest: The authors declare no conflict of interest.

References

1. Zhang, H.; Chen, X.Y.; Liu, Y.; Yang, C.Q.; Liu, W.Z.; Qi, M.Y.; Zhang, D. PDMS film-based flexible pressure sensor array with surface protruding structure for human motion detection and wrist posture recognition. *ACS Appl. Mater. Interfaces* **2024**, *16*, 2554–2563. [[CrossRef](#)]
2. Park, S.; Kim, B.; Jo, Y.; Dai, Z.; Lee, J. Chemiresistive trimethylamine sensor using monolayer SnO_2 inverse opals decorated with Cr_2O_3 nanoclusters. *Sens. Actuators B* **2024**, *309*, 127805. [[CrossRef](#)]
3. Li, Y.; Liu, J.Q.; Zhang, J.J.; Liang, X.; Zhang, X.S.; Qi, Q. Deposition of In_2O_3 nanofibers on polyimide substrates to construct high-performance and flexible trimethylamine sensor. *Chin. Chem. Lett.* **2020**, *31*, 2142–2144. [[CrossRef](#)]
4. Zhang, W.H.; Xu, P.; Shen, Y.P.; Feng, J.P.; Liu, Z.X.; Cai, G.; Yang, X.L.; Guan, R.F.; Su, L.X.; Yue, L. Selective detection of trimethylamine utilizing nanosheets assembled hierarchical $\text{WO}_{2.9}$ nanostructure. *J. Environ. Chem. Eng.* **2021**, *9*, 106493. [[CrossRef](#)]
5. Sui, X.; Zhang, D.; Wang, J.; Tang, M.; Xia, H.; Wang, Z. Ppb-level detection of trimethylamine as biomarker in exhaled gas based on $\text{MoO}_3/\text{V}_2\text{O}_5$ hierarchical heterostructure. *J. Alloys Compd.* **2023**, *968*, 172104. [[CrossRef](#)]
6. Zhang, D.Z.; Wu, Z.L.; Zong, X.Q. Flexible and highly sensitive H_2S gas sensor based on in-situ polymerized $\text{SnO}_2/\text{rGO}/\text{PANI}$ ternary nanocomposite with application in halitosis diagnosis. *Sens. Actuators B* **2019**, *289*, 32–41. [[CrossRef](#)]
7. Zhang, D.; Yang, Z.; Chen, H. Ozone gas sensing properties of metal-organic frameworks-derived In_2O_3 hollow microtubes decorated with ZnO nanoparticles. *Sens. Actuators B* **2019**, *301*, 127081. [[CrossRef](#)]
8. Pan, W.; Zhang, Y.; Yu, S.; Liu, X.; Zhang, D. Hydrogen sulfide gas sensing properties of metal organic framework-derived $\alpha\text{-Fe}_2\text{O}_3$ hollow nanospheres decorated with MoSe_2 nanoflowers. *Sens. Actuators B* **2021**, *334*, 130221. [[CrossRef](#)]
9. Guo, J.Y.; Zhang, D.Z.; Li, T.T.; Zhang, J.H.; Yu, L.D. Green light-driven acetone gas sensor based on electrospun CdS nanospheres/ Co_3O_4 nanofibers hybrid for the detection of exhaled diabetes biomarker. *J. Colloid Interface Sci.* **2022**, *606*, 261–271. [[CrossRef](#)] [[PubMed](#)]
10. Li, H.; Huang, L.; Wang, X.; Lee, C.; Yoon, J.; Zhou, J.; Guo, X.; Lee, J. Molybdenum trioxide nanopaper as a dual gas sensor for detecting trimethylamine and hydrogen sulfide. *RSC Adv.* **2017**, *7*, 3680–3685. [[CrossRef](#)]

11. Shen, S.; Zhang, X.; Cheng, X.; Xu, Y.; Gao, S.; Zhao, H.; Zhou, X.; Huo, L. Oxygen-vacancy-enriched porous α - MoO_3 nanosheets for trimethylamine sensing. *ACS Appl. Nano Mater.* **2019**, *2*, 8016–8026. [[CrossRef](#)]
12. Zhou, L.J.; Mi, Q.; Jin, Y.B.; Li, T.T.; Zhang, D.Z. Construction of $\text{MoO}_3/\text{MoSe}_2$ nanocomposite-based gas sensor for low detection limit trimethylamine sensing at room temperature. *J. Mater. Sci. Mater. Electron.* **2021**, *32*, 17301–17310. [[CrossRef](#)]
13. Yan, W.J.; Xu, H.S.; Ling, M.; Zhou, S.Y.; Qiu, T.; Deng, Y.J.; Zhao, Z.D. MOF-derived porous hollow $\text{Co}_3\text{O}_4/\text{ZnO}$ cages for high-performance MEMS trimethylamine sensors. *ACS Sens.* **2021**, *6*, 2613–2621. [[CrossRef](#)] [[PubMed](#)]
14. Zhang, B.; Liu, J.; Cui, X.B.; Wang, Y.L.; Gao, Y.; Sun, P.; Liu, F.M.; Shimano, K.; Yamazoe, N.; Lu, G.Y. Enhanced gas sensing properties to acetone vapor achieved by α - Fe_2O_3 particles ameliorated with reduced graphene oxide sheets. *Sens. Actuators B* **2017**, *241*, 904–914. [[CrossRef](#)]
15. Liu, J.B.; Hu, J.Y.; Liu, C.; Tan, Y.M.; Zhang, Y. Mechanically exfoliated MoS_2 nanosheets decorated with SnS_2 nanoparticles for high-stability gas sensors at room temperature. *Rare Met.* **2020**, *40*, 1536–1544. [[CrossRef](#)]
16. Pan, Q.N.; Li, T.T.; Zhang, D.Z. Ammonia gas sensing properties and density functional theory investigation of coral-like Au-SnSe_2 Schottky junction. *Sens. Actuators B* **2021**, *332*, 129440. [[CrossRef](#)]
17. Zhang, H.; Zhang, D.Z.; Zhang, B.; Wang, D.Y.; Tang, M.C. Wearable pressure sensor array with layer-by-layer assembled MXene nanosheets/Ag nanoflowers for motion monitoring and human-machine interfaces. *ACS Appl. Mater. Interfaces* **2022**, *14*, 48907–48916. [[CrossRef](#)] [[PubMed](#)]
18. Wang, D.Y.; Zhang, D.Z.; Yang, Y.; Mi, Q.; Zhang, J.H.; Yu, L.D. Multifunctional latex/polytetrafluoroethylene-based triboelectric nanogenerator for self-powered organ-like MXene/metal-organic framework-derived CuO nanohybrid ammonia sensor. *ACS Nano* **2021**, *15*, 2911–2919. [[CrossRef](#)]
19. Zhang, H.; Zhang, D.; Wang, Z.H.; Xi, G.S.; Mao, R.Y.; Ma, Y.H.; Wang, D.Y.; Tang, M.C.; Xu, Z.Y.; Luan, H.X. Ultrastretchable, self-healing conductive hydrogel-based triboelectric nanogenerators for human-computer interaction. *ACS Appl. Mater. Interfaces* **2023**, *15*, 5128–5138. [[CrossRef](#)]
20. Liu, M.; Ding, Y.; Lu, Z.; Song, P.; Wang, Q. Layered $\text{Ti}_3\text{C}_2\text{T}_x$ MXene/ CuO spindles composites for NH_3 detection at room temperature. *J. Alloy Compd.* **2023**, *938*, 168563. [[CrossRef](#)]
21. Pasupuleti, K.; Thomas, A.; Vidyasagar, D.; Rao, V.; Yoon, S.; Kim, Y.; Kim, S.; Kim, M. $\text{ZnO}@\text{Ti}_3\text{C}_2\text{T}_x$ MXene hybrid composite-based Schottky-barrier-coated SAW sensor for effective detection of sub-ppb-level NH_3 at room temperature under UV illumination. *ACS Mater. Lett.* **2023**, *5*, 2739–2746. [[CrossRef](#)]
22. Peng, J.H.; Chen, X.Z.; Ong, W.J.; Zhao, X.J.; Li, N. Surface and heterointerface engineering of 2D MXenes and their nanocomposites: Insights into electro- and photocatalysis. *Chem* **2019**, *5*, 18–50. [[CrossRef](#)]
23. Zou, S.; Gao, J.; Liu, L.M.; Lin, Z.D.; Fu, P.; Wang, S.G.; Chen, Z. Enhanced gas sensing properties at low working temperature of iron molybdate/MXene composite. *J. Alloys Compd.* **2020**, *817*, 152785. [[CrossRef](#)]
24. He, T.T.; Liu, W.; Lv, T.; Ma, M.S.; Liu, Z.F.; Vasiliev, A.; Li, X.G. MXene/ SnO_2 heterojunction based chemical gas sensors. *Sens. Actuators B* **2021**, *329*, 129275. [[CrossRef](#)]
25. Zhang, D.Z.; Yu, S.J.; Wang, X.W.; Huang, J.K.; Pan, W.J.; Zhang, J.H.; Meteku, B.E.; Zeng, J.B. UV illumination-enhanced ultrasensitive ammonia gas sensor based on (001) $\text{TiO}_2/\text{MXene}$ heterostructure for food spoilage detection. *J. Hazard. Mater.* **2022**, *423*, 127160. [[CrossRef](#)]
26. Gatty, H.; Leijonmarck, S.; Antelius, M.; Stemme, G.; Roxhed, N. An amperometric nitric oxide sensor with fast response and ppb-level concentration detection relevant to asthma monitoring. *Sens. Actuators B* **2015**, *209*, 639–644. [[CrossRef](#)]
27. Nakate, U.; Yu, Y.; Park, S. Hydrothermal synthesis of ZnO nanoflakes composed of fine nanoparticles for H_2S gas sensing application. *Ceram. Int.* **2022**, *19*, 28822–28829. [[CrossRef](#)]
28. Zhen, Y.; Zhao, Q.; Duan, Z.; Xie, C.; Duan, X.; Li, S.; Ye, Z.; Jiang, Y.; Tai, H. Ag_2Te nanowires for humidity-resistant trace-level NO_2 detection at room temperature. *Sens. Actuators B* **2022**, *363*, 131790.
29. Wang, X.; Zhang, Y.; Chen, Z. Effect of MoO_3 constituents on the growth of MoS_2 nanosheets by chemical vapor deposition. *Mater. Res. Express* **2016**, *3*, 065014. [[CrossRef](#)]
30. Ma, X.; Tu, X.L.; Gao, F.; Xie, Y.; Huang, X.G.; Fernandez, C.; Qu, F.L.; Liu, G.B.; Lu, L.M.; Yu, Y.F. Hierarchical porous MXene/amino carbon nanotubes-based molecular imprinting sensor for highly sensitive and selective sensing of fisetin. *Sens. Actuators B* **2020**, *309*, 127815. [[CrossRef](#)]
31. Liu, L.J.; Zhao, Q.; Liu, R.; Zhu, L.F. Hydrogen adsorption-induced catalytic enhancement over Cu nanoparticles immobilized by layered Ti_3C_2 MXene. *Appl. Catal. B* **2019**, *252*, 198–204. [[CrossRef](#)]
32. Han, M.K.; Yin, X.W.; Wu, H.; Hou, Z.X.; Song, C.Q.; Li, X.L.; Zhang, L.T.; Cheng, L.F. Ti_3C_2 MXenes with modified surface for high-performance electromagnetic absorption and shielding in the X-band. *ACS Appl. Mater. Interfaces* **2016**, *8*, 21011–21019. [[CrossRef](#)]
33. Meng, D.; Liu, D.; Wang, S.; Shen, Y.; San, X.; Si, J.; Meng, F. In-situ growth of ordered Pd-doped ZnO nanorod arrays on ceramic tube with enhanced trimethylamine sensing performance. *Appl. Surf. Sci.* **2019**, *463*, 348–356. [[CrossRef](#)]
34. Wang, D.; Gu, K.; Zhao, Q.; Zhai, C.; Yang, T.; Lu, Q.; Zhang, J.; Zhang, M. Synthesis and trimethylamine sensing properties of spherical V_2O_5 hierarchical structures. *N. J. Chem.* **2018**, *42*, 14188. [[CrossRef](#)]
35. Meng, D.; Si, J.; Wang, M.; Wang, G.; Shen, Y.; San, X.; Meng, F. One-step synthesis and the enhanced trimethylamine sensing properties of $\text{Co}_3\text{O}_4/\text{SnO}_2$ flower-like structures. *Vacuum* **2020**, *171*, 108994. [[CrossRef](#)]

36. Ma, Z.; Song, P.; Yang, Z.; Wang, Q. Trimethylamine detection of 3D rGO/mesoporous In₂O₃ nanocomposites at room temperature. *Appl. Surf. Sci.* **2019**, *465*, 625–634. [[CrossRef](#)]
37. Mounasamy, V.; Mani, G.; Ponnusamy, D.; Tsuchiya, K.; Prasad, A.; Madanagurusamy, S. Sub-ppm level detection of trimethylamine using V₂O₃-Cu₂O mixed oxide thin films. *Ceram. Int.* **2019**, *45*, 19528–19533. [[CrossRef](#)]
38. Li, Z.; Lou, C.; Lei, G.; Lu, G.; Pan, H.; Liu, X.; Zhang, J. Atomic layer deposition of Rh/ZnO nanostructures for anti-humidity detection of trimethylamine. *Sens. Actuators B* **2022**, *355*, 131347. [[CrossRef](#)]
39. Qiao, X.; Zhang, Z.; Hou, D.; Li, D.; Liu, Y.; Lan, Y.; Zhang, J.; Feng, P.; Bu, X. Tunable MoS₂/SnO₂ P-N heterojunctions for an efficient trimethylamine gas sensor and 4-nitrophenol reduction catalyst. *ACS Sustain. Chem. Eng.* **2018**, *6*, 12375–12384. [[CrossRef](#)]

Disclaimer/Publisher’s Note: The statements, opinions and data contained in all publications are solely those of the individual author(s) and contributor(s) and not of MDPI and/or the editor(s). MDPI and/or the editor(s) disclaim responsibility for any injury to people or property resulting from any ideas, methods, instructions or products referred to in the content.